

High-Quality Mesh Blendshape Generation from Face Videos via Neural Inverse Rendering

Xin Ming^{1*}, Jiawei Li^{2*}, Jingwang Ling¹, Libo Zhang¹, Feng Xu¹

¹ Tsinghua University ² Hong Kong University of Science and Technology

Abstract

Readily editable mesh blendshapes have been widely used in animation pipelines, while recent advancements in neural geometry and appearance representations have enabled high-quality inverse rendering. Building upon these observations, we introduce a novel technique that reconstructs mesh-based blendshape rigs from single or sparse multi-view videos, leveraging state-of-the-art neural inverse rendering. We begin by constructing a deformation representation that parameterizes vertex displacements into differential coordinates with tetrahedral connections, allowing for high-quality vertex deformation on high-resolution meshes. By constructing a set of semantic regulations in this representation, we achieve joint optimization of blendshapes and expression coefficients. Furthermore, to enable a user-friendly multi-view setup with unsynchronized cameras, we propose a neural regressor to model time-varying motion parameters. This approach implicitly considers the time difference across multiple cameras, enhancing the accuracy of motion modeling. Experiments demonstrate that, with the flexible input of single or sparse multi-view videos, we reconstruct personalized high-fidelity blendshapes. These blendshapes are both geometrically and semantically accurate, and they are compatible with industrial animation pipelines. Code and data will be released.

1. Introduction

Synthesizing realistic 3D facial animations has long held significant applications in the movie and gaming industry. Accurate modeling of facial geometry and expression deformation constitutes a fundamental challenge for this task. In the industry, modeling usually involves a studio-level multi-view setup [3, 16, 24] to capture facial performances of real humans, along with the artist’s manual effort to generate a facial rig. This facial rig is then imported into an anima-



Figure 1. With the input of sparse multi-view face videos (shown on the left), our technique reconstructs personalized mesh-based blendshapes (examples shown on the right) that are ready to be used in the industrial animation pipeline.

tion pipeline [15, 56] for game and movie production. VR and AR applications further require modeling facial rigs for a vast user base, necessitating an automated approach for facial modeling from widespread capture setups. One critical requirement is that the modeled face rig must be compatible with the animation pipeline to enable downstream animation applications.

RGB cameras are prevalent on everyday mobile devices, making them a popular choice for user-friendly facial reconstruction in numerous works. In addition to detecting facial landmarks from RGB inputs to fit facial statistical models [9, 10, 52], differentiable rendering [27] can improve the reconstruction fidelity by harnessing dense pixel observations. However, overly-simplified rendering models cause under-fitting of facial material and arbitrary lighting, thereby negatively impacting the shape reconstruction quality. With the recent advancements in neural inverse rendering [38, 51], techniques like neural facial avatars [19, 25, 66, 68, 69] can generate realistic animatable avatars from common RGB recordings. However, these techniques do not rely on high-quality topology-consistent mesh rep-

* Both authors contributed equally to the paper

resentation and thus are not compatible with the industrial animation pipeline, impacting their practical utility. To bridge the gap between realistic modeling and compatibility with current animation pipelines using easy recording setups, we, on one hand, represent dynamic facial modeling as a blendshape rig [31], consisting of topology-consistent facial meshes for various expressions. On the other hand, we optimize the blendshape with novel per-vertex deformation schemes to precisely match the generated animation to the facial performance in RGB videos (inverse rendering). Once converged, the obtained blendshape can be imported into animation software (e.g. Blender [14]) to generate realistic person-specific facial animations for industrial applications.

To achieve high-quality shape reconstruction and animation by optimizing the blendshape rig via neural inverse rendering, we propose techniques to solve three unaddressed issues. The first arises in optimizing per-vertex deformations of a high-resolution mesh, which can be non-smooth and suffer from self-intersections. By applying differential coordinates to parameterize blendshape meshes augmented with tetrahedral connections, we facilitate gradient propagation along topologically and spatially adjacent vertices, ensuring smooth deformation. Secondly, there is an ambiguity in optimizing either expression bases or coefficients to fit users’ arbitrary facial performance, and prior methods [19, 25, 69] typically circumvent this by excluding expression coefficients from the optimization (estimating them through a pre-processing step [52]) thus only reaching local optimums. We aim to improve convergence by joint optimization with novel regularization techniques that enforce the symmetry, sparsity, and semantics of expression bases to solve the ambiguity. Thirdly, multi-view inputs are useful for accurately reconstructing non-rigid facial deformations [20], but previous research usually does not presume that multi-view inputs are readily available, as they are typically linked with complex procedures such as synchronization and color correction. We incorporate sparse multi-view inputs from unsynchronized smartphones by proposing a neural regressor to model time-dependent motion parameters, implicitly ensuring temporal synchronization. We achieve efficient optimization that reconstructs a facial rig in 15 minutes. In summary, our contributions include:

- A video-based facial rigging technique that bridges traditional animation pipelines and neural inverse rendering to achieve high-quality animation-ready facial rig reconstruction from single or sparse multi-view videos,
- a novel blendshape deformation technique that parameterizes differential coordinates augmented with tetrahedral connections, involving a set of semantic regularization into a joint optimization, and
- a neural regressor modeling time-varying motion parameters to achieve implicit time synchronization across mul-

iple views.

2. Related Work

3D Facial Performance Capture. Many studies have been devoted to generating realistic 3D animations from users’ facial performance. High-quality facial animation can be reconstructed through a studio-level multi-view setup as demonstrated in [3, 7, 18]. However, this involves intricate procedures for dozens of professional cameras, including synchronization and color correction. To enable facial performance capture using ubiquitous devices, [9, 10, 59] fit morphable models [5, 57] from monocular RGB or RGBD videos. To achieve a more personalized facial geometry beyond the morphable model, [11, 22, 37] introduce fine-level displacements on the facial mesh to synthesize nuanced facial details. Due to the inherent ambiguity in non-rigid facial reconstruction from monocular input, deformation is highly constrained. In attempts to address such limitation, [12, 55] extend to sparse views and observe reconstruction improvements. Establishing a simple and user-friendly sparse view setup remains an active research topic. While the aforementioned approaches can reconstruct dynamic facial geometries, additional efforts are required to organize the performance data into a facial rig for convenient editing and synthesis of novel facial animations.

3D Facial Rigging. Rigging aims to generate a personalized facial expression model from the user’s performance, typically represented using blendshapes [31] for compatibility with the animation pipeline. [49] can personalize template blendshapes from a neutral expression mesh. Furthermore, [34, 65] utilize data-driven priors to predict personalized expression bases from a neutral scan or image. To achieve higher degrees of personalization from more observations, [32] takes input from multiple scans with predefined expressions, while [26] requires users to make specific key expressions during the capture process. Exploring more user-friendly capture procedures, [6, 23, 33, 58] focus on utilizing performance sequences where users make arbitrary facial expressions to generate expression blendshapes. Updating blendshapes requires careful design to avoid mesh non-smoothness, thus techniques such as reduced subspace [6] and corrective shapes [23, 33] are employed to constrain deformations. To resolve the ambiguity between expression bases and expression coefficients, [58] proposes semantic emotion priors to constrain expressions. Our work introduces a vertex deformation representation that enables high-fidelity deformation of blendshapes while enforcing smoothness. We also design constraints to maintain semantic coherence in expression blendshapes.

Neural Inverse Rendering. Differentiable rendering [30, 36, 43] can leverage gradient backpropagation to optimize geometry, material and lighting to achieve inverse rendering-based reconstruction. Facial materials, influ-

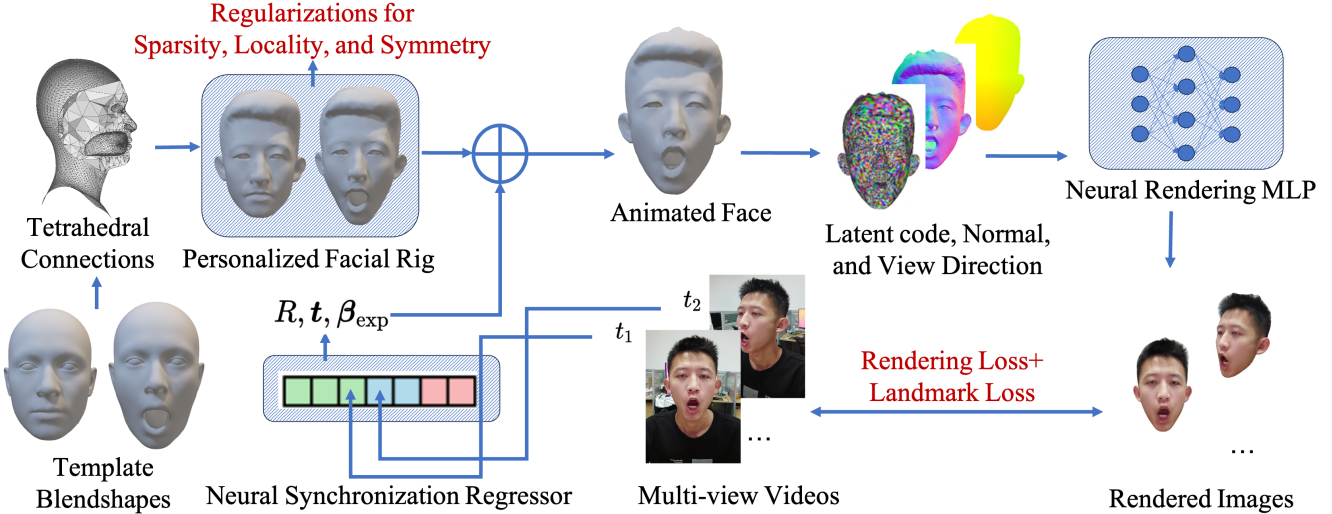


Figure 2. The overview of our method.

enced by subsurface scattering [17], are challenging to represent using simplified rendering models, which can lead to underfitting in differentiable rendering. Recent advances in neural rendering [38, 53, 60] bypass this limitation by directly modeling the emitting radiance via neural networks, achieving realistic novel-view synthesis [38, 53] and reconstruction [60] of static objects. [8, 45] achieve dynamic object modeling via neural deformation fields, but do not incorporate expression-driven retargeting. [2, 19, 21, 64, 69] extend NeRF [38] to expression-driven dynamic faces. However, the density-based representation employed by their methods lacks explicit geometric regularization, often lowering the quality of novel views. [66, 68] explore alternative representations such as implicit fields and point clouds, but compatibility with animation pipelines remains a challenge. [25] can obtain a mesh representation after a long training time, but with a primary focus on rendering quality rather than accurate geometry reconstruction, frequently leading to details being baked in textures. Concurrently and independently, [4] explores the use of mesh-based representation for fast learning of facial avatars. Compared to their works, our emphasis lies more on the geometric quality and compatibility of animation. Therefore, we jointly optimize blendshapes and expression coefficients, incorporate regularization to maintain the semantics of the updated blendshapes, and achieve accurate reconstruction evaluated by point-to-plane distance.

3. Method

We aim to reconstruct personalized mesh-based blendshapes from RGB videos. Personalization involves per-vertex deformation applied to the blendshapes. We propose a deformation representation, outlined in Sec. 3.1, to

ensure smoothness and prevent self-intersection for high-resolution meshes. Based on the representation, the deformations are further regularized, introduced in Sec. 3.2, to maintain the semantics of the expression blendshapes. The sparse multi-view inputs, which are used to guide the deformations, are implicitly synchronized by a neural synchronization regressor illustrated in Sec. 3.3. Additionally, with a neural rendering pipeline in Sec. 3.4 to render the animated faces, we compare the rendered faces with the input to reconstruct the blendshape deformation. To be specific, the reconstruction is solved by the joint optimization of the blendshape deformation, the rendering network, and the synchronization regressor in Sec. 3.5. Fig. 2 represents an overview of our method.

3.1. Vertex Deformations with Tetrahedral Connections

The facial shape is represented by a mesh where a morphable model [5] describes its identity variations and blendshapes [31] describe its expression deformation. An identity PCA model $B_{\text{id}} \in \mathbb{R}^{3N \times M_{\text{id}}}$ represents neutral faces with different identities. A face with neutral expression can be obtained as $\mathbf{b}_n = \mathbf{b}_\mu + B_{\text{id}} \beta_{\text{id}}$ given a set of coefficients $\beta_{\text{id}} \in \mathbb{R}^{M_{\text{id}}}$ and the mean face $\mathbf{b}_\mu \in \mathbb{R}^{3N}$. Similarly, a blendshape model represents a face with a specific expression as $\mathbf{b}_\beta = \mathbf{b}_n + B_{\text{exp}} \beta_{\text{exp}}$, where \mathbf{b}_n denotes the user-specific neutral face, $B_{\text{exp}} \in \mathbb{R}^{3N \times M_{\text{exp}}}$ denotes the blendshape model, and $\beta_{\text{exp}} \in \mathbb{R}^{M_{\text{exp}}}$ represents the expression coefficients. Our objective is to generate a person-specific facial rig consisting of a neutral face \mathbf{b}_n^* and a set of blendshapes B_{exp}^* by solving per-vertex deformation applied to \mathbf{b}_n and B_{exp} .

However, directly optimizing per-vertex deformation

poses challenges for convergence [40]. To ensure smoothness and prevent self-intersection cavities, we devise a vertex parameterization that implicitly satisfies volumetric Laplacian regularization. First, we parameterize vertex displacements into differential coordinates [48], inspired by [40]. The parameterization propagates vertex gradients to neighboring vertices based on mesh connectivity, effectively enforcing smooth deformation. However, there is no gradient propagation between spatially adjacent but not directly connected vertices, and mesh self-intersection can still occur. Therefore, we augment mesh connectivity via internal tetrahedral filling. Specifically, we use TetGen [46] to fill the closed space between the surface and corresponding internal sockets with tetrahedras, preventing interpenetration due to large deformations. We use Φ to denote the process of tetrahedralizing and reparameterizing per-vertex deformation. The personalized neutral face is represented as $\mathbf{b}_n^* = \Phi(\mathbf{b}_n)$. Blendshapes are deformed similarly as $B_{\text{exp}}^* = \Phi(B_{\text{exp}})$.

Discussion. [25, 68] employ MLPs to regress deformations from canonical vertex coordinates, observing that the output deformations exhibit spatial smoothness. We attribute this phenomenon to the shared network among vertices, where during backpropagation, the gradient of one vertex influences others, with a greater impact on adjacent vertices [50]. We have employed a network-free method that achieves similar effects, propagating vertex gradients to topologically and spatially adjacent vertices. This approach is memory-efficient, faster, and suitable for applications with multiple ($M_{\text{exp}} = 53$) blendshape bases.

3.2. Rigging Regularization

Blendshapes have clear semantics due to their connection with facial action units [42]. However, the semantics may be corrupted due to ambiguity as we optimize both expression coefficients β_{exp} and blendshapes B_{exp}^* simultaneously. To this end, we propose regularizations based on three principles, namely locality, sparsity, and symmetry, to ensure that we obtain a semantically consistent rig.

Locality. Each blendshape corresponds to an action unit, and its deformation has a localized influence region. The update of a blendshape should be concentrated on its original activation region. To this end, we first compute the per-vertex deforming weights based on the initial blendshapes given by

$$W = \exp\left(-\frac{\|B_{\text{exp}}\|_2}{a}\right) \quad (1)$$

where a is a hyperparameter controlling the smoothness of the activation region boundary.

The weight is used to compute the locality loss defined as

$$\mathcal{L}_{\text{locality}} = \|(W \odot \|B_{\text{exp}}^* - B_{\text{exp}}\|_2)\|_1 \quad (2)$$

where \odot denotes element-wise multiplication.

Sparsity. The dynamic facial deformation should be explained by only a few blendshapes. The sparsity loss is defined as:

$$\mathcal{L}_{\text{sparsity}} = \|B_{\text{exp}}^* - B_{\text{exp}}\|_p \quad (3)$$

with $p < 1$. We use $p = 0.75$ in the experiments.

Symmetry. The blendshapes which are symmetric for the left and right faces should still maintain symmetry. We manually select the symmetric ones from the initial blendshapes, and only update their left half faces. The right half faces are obtained by symmetry.

3.3. Sparse Multi-View Handling

Accurate modeling of dynamic faces from monocular videos is an ill-posed problem [20]. However, increasing the number of viewpoints often incurs cumbersome setups such as synchronization. Conversely, we allow unsynchronized RGB videos captured from mobile phones as input. To address the issue of incomplete time synchronization among multiple devices, we propose to use a one-dimensional Instant-NGP[39] to store temporal information to implicitly ensure synchronization. Specifically, for each viewpoint k , we record the video start time t_s^k from the system clock of the mobile phone. The time of the i th frame can be calculated as $t_i^k = t_s^k + \frac{i}{r_k}$, where r_k is the frame rate. t_i^k will be used to regress parameters containing face rotation R_i^k , translation t_i^k , and expression coefficients β_i^k with the neural regressor as:

$$R_i^k, t_i^k, \beta_i^k = \text{Grid}(t_i^k) \quad (4)$$

Compared to another viewpoint k' , while t_i^k and $t_i^{k'}$ are not captured at the same time, they have independent motion parameters, and the neural regressor ensures smoothness for temporally close parameters.

To address the exposure difference among different viewpoints, we assign a learnable latent code for each camera \mathbf{h}_k when rendering. Details will be explained in the next section.

3.4. Mesh-based Neural Deferred Rendering

Mesh-based face models enable us to perform efficient rendering using differentiable rasterization [30]. However, overly simplified rendering models may suffer from underfitting due to the complex material of the face and arbitrary lighting. Motivated by [61], We use a technique that combines neural rendering and deferred rendering from real-time rendering pipelines. Specifically, a latent code is assigned to each mesh vertex, which represents the neural texture. In the rendering process, the mesh is first rasterized, yielding the triangle indices and barycentric coordinates for each pixel, which are used to interpolate the latent codes,

vertex normals and view directions. Then, we use a learnable MLP-based shader to regress the per-pixel RGB color:

$$f_{\theta}(z, \mathbf{n}, \omega, \mathbf{h}_k) \in [0, 1]^3 \quad (5)$$

where z denotes the latent code, \mathbf{n} denotes the normal, ω denotes the view direction, \mathbf{h}_k denotes the learnable latent code assigned to the k -th viewpoint and θ denotes the network parameters.

3.5. Joint Optimization

Our optimization objective integrates multiple loss components to collectively optimize all trainable parameters from randomly initialized values, including the facial rig, the neural regressor, and the neural shader. The formulation of the joint optimization objective is expressed as follows:

$$\begin{aligned} \mathcal{L}_{\text{total}} = & \mathcal{L}_{\text{ldmk}} + \mathcal{L}_{\text{mask}} + \mathcal{L}_{\text{photometric}} \\ & + \mathcal{L}_{\text{Laplacian}} + \mathcal{L}_{\text{locality}} \\ & + \mathcal{L}_{\text{sparsity}} + \mathcal{R}_{\text{shape\&exp}} + \mathcal{R}_{\text{neutral}} \end{aligned} \quad (6)$$

This objective function encapsulates various aspects, including landmark loss $\mathcal{L}_{\text{ldmk}}$, mask loss $\mathcal{L}_{\text{mask}}$, photometric loss $\mathcal{L}_{\text{photometric}}$, Laplacian loss $\mathcal{L}_{\text{Laplacian}}$, shape and expression regularization $\mathcal{R}_{\text{shape\&exp}}$, and regularization for template deformation $\mathcal{R}_{\text{neutral}}$. $\mathcal{L}_{\text{sparsity}}$ and $\mathcal{L}_{\text{locality}}$ have been explained in the previous section. $\mathcal{L}_{\text{ldmk}}$ enforces accurate prediction of facial landmarks, while $\mathcal{R}_{\text{shape\&exp}}$ constrain extreme deformations.

$$\mathcal{L}_{\text{ldmk}} = \frac{1}{N} \sum_{i=1}^N \|\hat{v}_i - v_i\|_1 \quad (7)$$

where \hat{v} indicates the landmarks projected on images and v indicates the detected N landmarks.

$$\mathcal{R}_{\text{shape\&exp}} = \|\beta_{\text{id}}\|_2^2 + \|\beta_{\text{exp}}\|_1 \quad (8)$$

where β_{id} is the identity coefficient and β_{exp} is the expression coefficient. $\mathcal{L}_{\text{mask}}$ ensures the alignment of rendered masks \hat{M} and segmented masks M , and $\mathcal{L}_{\text{photometric}}$ enforces consistency between rendered images \hat{I} and captured images I

$$\mathcal{L}_{\text{mask}} = \|\hat{M} - M\|_1 \quad (9)$$

$$\mathcal{L}_{\text{photometric}} = \|M \odot (\hat{I} - I)\|_1 \quad (10)$$

where \odot denotes element-wise multiplication. $\mathcal{L}_{\text{Laplacian}}$ enforces smoothness of latent codes between adjacent vertices.

$$\mathcal{L}_{\text{Laplacian}} = \|L\mathbf{u}\|_2^2 \quad (11)$$

where L is the Laplacian matrix and \mathbf{u} denotes the per-vertex latent code. $\mathcal{R}_{\text{neutral}}$ constrains deformation of the neutral face.

$$\mathcal{R}_{\text{neutral}} = \|\mathbf{b}_n^* - \mathbf{b}_n\|_2^2 \quad (12)$$

This comprehensive optimization objective facilitates the joint refinement of our pipeline. In our experiment, the $\mathcal{L}_{\text{ldmk}}$ (including the landmarks on eye balls) and $\mathcal{R}_{\text{shape\&exp}}$ are initially activated to obtain a coarse alignment. After a number of epochs, we proceed to enable all the loss components.

4. Experiments

In this section, we first describe the implementation details of our method and provide information about the used datasets. Next, we qualitatively and quantitatively compare the accuracy of geometric reconstruction with previous works. We then conduct ablation studies to assess the impact of the deformation representation on vertex optimization and the role of semantic regularization in constraining expression bases. Finally, we demonstrate the application of our method in animation, including expression retargeting and novel-view synthesis. More results can be found in our supplementary document and video.

4.1. Implementation Details

For the input videos, we use Facer [67] to obtain the facial landmarks and masks. We use a three-layer MLP as the neural renderer, which has 64 hidden units and uses ReLU as the activation function. In the hierarchical grids of our neural synchronization regressor, we use 6 grid scales with a base resolution of 8, and we use 4 channels per level. We use Nvdiffrast [30] as the differentiable rasterizer. For the neural renderer and the regressor, we use an Adam [28] optimizer with $\eta = 1e^{-3}$ and $\beta = (0.9, 0.999)$. The facial rig is updated using an AdamUniform [40] optimizer, with the same parameters as the Adam optimizer. We train our model for 200 epochs, with all loss functions activated for the last 120 epochs.

To establish tetrahedral connections, we use Blender [14] to preprocess the template neutral blendshape of the ICT face model [35], constructing a small closed volume space between the surface and the corresponding internal sockets. Next, we use TetGen [46] to fill this closed space with tetrahedras, creating edges between the surface vertices and the internal socket vertices. After performing this for the neutral expression, we deformed it using the ARAP [47] to align with the 53 expression blendshapes and 100 identity bases in the ICT, ensuring that all blendshapes are filled with tetrahedral connections of consistent topology.

4.2. Datasets and Metrics

Datasets We capture our dataset using four mobile phones for qualitative comparisons. Additionally, we conduct qualitative and quantitative evaluations on the Multiface [63] and NeRSemble [29] datasets, which feature high-quality multi-view captures of different identities with rich expressions. We utilize MetaShape [1] to reconstruct accurate 3D

point-to-plane error(mm)	Multiface		NeRSemble	
	Mean	Std	Mean	Std
NHA	3.76	0.13	4.98	0.36
PointAvatar	7.66	0.28	7.22	0.34
Ours	2.31	0.05	2.73	0.26

Table 1. Quantitative comparison in point-to-plane errors among NHA, PointAvatar, and our method on the NeRSemble and MultiFace datasets.

scans from all available views of the two datasets (38 in [63] and 16 in [29]) as the ground truth. For each dataset, we manually select four views as the inputs to simulate the sparse-view setup. All experiments in the main paper are conducted with four-view inputs. We present the experimental results under a single view in the supplementary materials to demonstrate that our method is also applicable for easier setup, and additionally compare the geometric reconstruction errors between sparse multi-view and single-view inputs.

Evaluation Metrics We adopt the evaluation metrics from [62] to compute point-to-plane L2 errors at facial regions between reconstructed 3D shapes and ground-truth 3D scans. We report reconstruction errors averaged across all frames in a video sequence.

4.3. Comparisons

To evaluate the accuracy of the geometric reconstruction, we perform qualitative and quantitative comparisons on the reconstruction results using the Multiface [63] and NeRSemble [29] datasets. We choose to compare NHA [25] and PointAvatar [68] as they represent the latest works on face avatars based on explicit shape representation. PointAvatar [68] claims to achieve higher synthesis quality compared to [66]. Works such as [2, 19, 21, 64, 69] achieve high-quality rendering, but their density-based representations are not suitable for direct comparisons. We modified the baselines so that all methods use input from four views. As shown in Table 1, our method surpasses other methods in point-to-plane errors on both datasets. Lower errors are also evident in the visualized heatmaps in Fig. 3, where we achieve more accurate reconstruction, especially in the eye and nose regions. In Fig. 4, a qualitative comparison of the reconstruction results for identity and expression-specific facial details is presented. In the first row, our method reconstructs a more personalized puckering expression. In the second row, our method successfully reconstructs the aquiline nose, which is a distinctive geometric feature specific to the input identity.

4.4. Ablation Study

To test the necessity of the blendshape deformation representation in preserving the mesh’s desirable properties, we

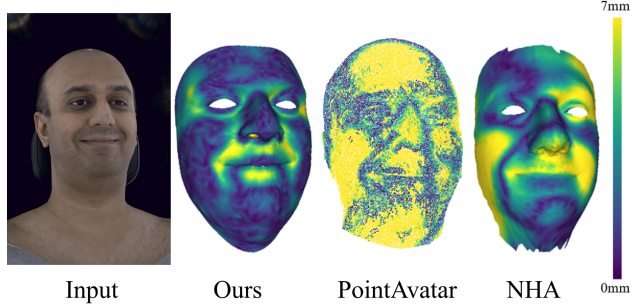


Figure 3. Visualization of the point-to-plane error heatmaps for NHA, PointAvatar, and our method.

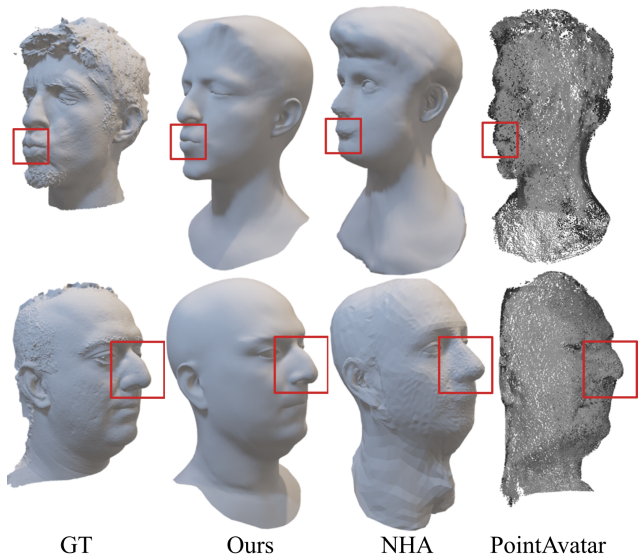


Figure 4. Comparisons of identity and expression-related facial details between our method and other baselines.

present geometric reconstruction results under different settings. We compare the reconstruction results of our method with: (1) without using differential coordinates and (2) with tetrahedral connections disabled. The results are then compared against the full pipeline. As shown in the upper row of Fig. 6, the utilization of differential coordinates in the optimization process significantly enhances the smoothness of the face surface, effectively eliminating numerous artifacts. The lower row in Fig. 6 illustrates the results of using tetrahedral connections during the vertex deformation process. When the user exhibits extreme facial expressions, such as a puckered mouth, there is a risk of penetration between the mouth socket and the facial surface, especially for high-resolution meshes. By establishing tetrahedral connections between surface points and internal socket points, we effectively mitigated the penetration without compromising the

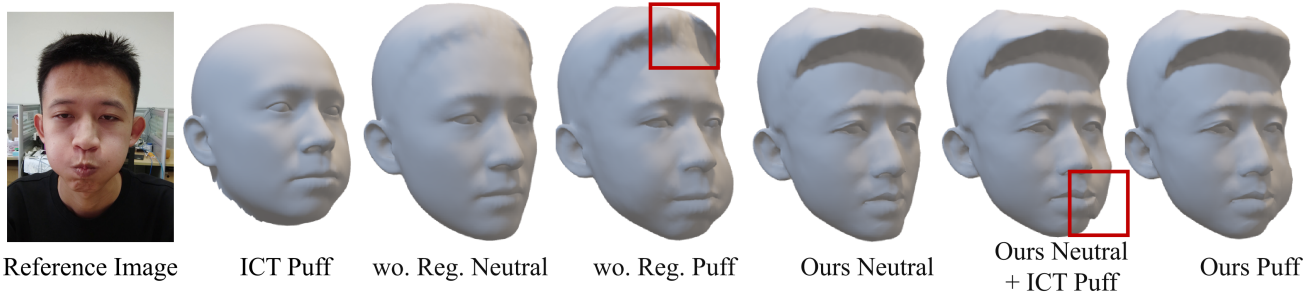


Figure 5. Blendshapes of neutral and cheek puffing expressions obtained by different solutions. The results reveal that our method not only correctly encodes the identity information in the neutral blendshape but also encodes the single-sided puffing expression in its corresponding blendshape.

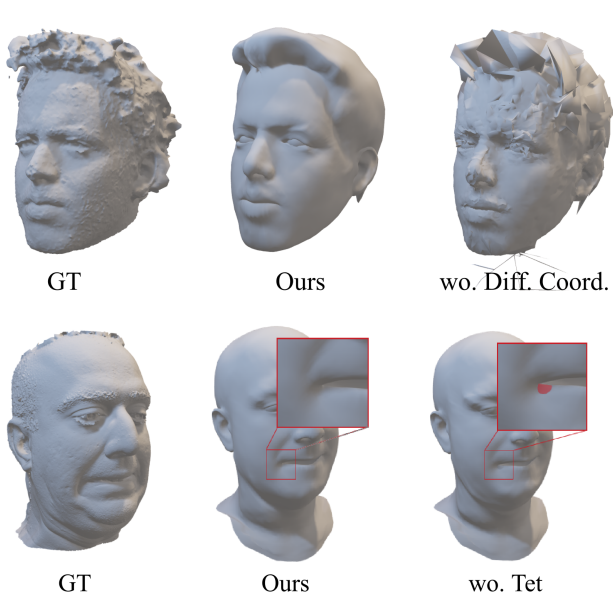


Figure 6. Evaluating the effectiveness of the blendshape deformation representation, including differential coordinate reparameterization and tetrahedral connections.

accuracy of deformation.

To evaluate the impact of blendshape updates and semantic regularization in the updates, we visualize the obtained expression bases under different settings in Fig. 5. The first column showcases a frame from the input sequence where the user makes a puffy expression. Our objective is to update the personalized one-sided puffy expression basis based on the inputs. If expressions are made only in the expression space of the ICT morphable model (second column), the resulting face deviates significantly from the user’s identity, lacking personalization. If the expression basis is updated without applying semantic regularization, identity-specific hair details are missing on the neutral face (third column). The relevant detail components appear in-

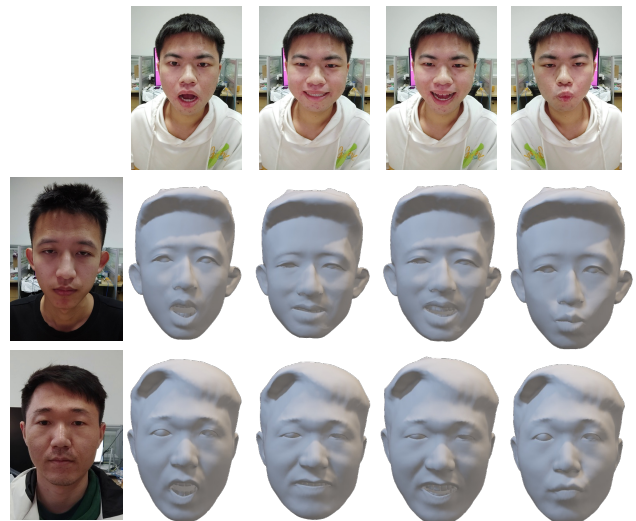


Figure 7. Retargeting results of our personalized facial rig. The first row shows the source expressions. The following rows show the retargeting results, where the images in the first column show the neutral expression of the target identities.

appropriately in the expression basis (fourth column, highlighted by red boxes). When applying semantic regularization, our method can reconstruct a high-quality neutral face (fifth column) that includes all identity-related facial details. However, if the expression basis is not updated and template blendshapes are directly applied to deform the personalized neutral face, artifacts due to mismatched deformations occur in the deformed region (sixth column, highlighted by red boxes). After updating the expression basis and applying semantic regularization, our method synthesizes high-quality personalized expression bases (seventh column).

4.5. Applications

In this section, we showcase the animation applications of the reconstructed results, including expression retargeting

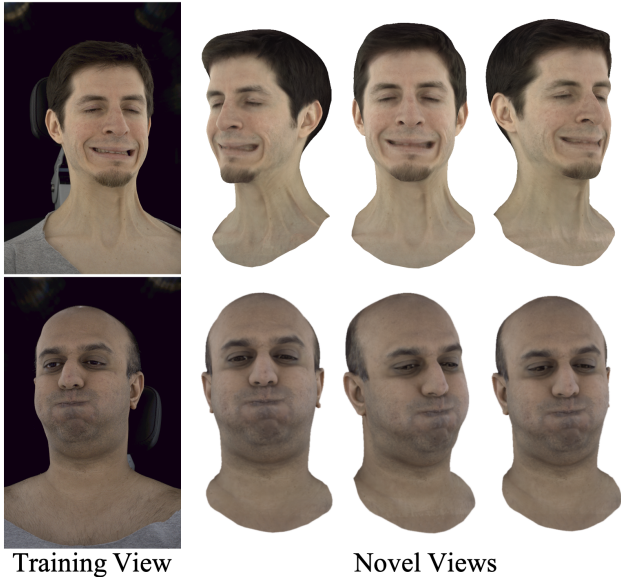


Figure 8. Results of novel view synthesis for an input frame of our method.

and novel-view synthesis.

Expression retargeting. The reconstructed geometry, represented by blendshapes with consistent topology, adheres to the format of animation pipelines. Therefore, it can be directly imported into animation software (such as Blender[14]) for synthesizing expressive animations, as depicted in Fig. 7. We demonstrate the results of the reconstructed facial rig being driven by a performer of a different identity. During a puckering expression, our method synthesizes distinct lip shapes between individuals (fourth column), and during a grimace, we observe person-specific nasolabial folds (third column). Expression-related nasolabial folds are properly deactivated when the skin is relaxed (fourth column). Our facial rig includes complete teeth that can be properly driven (second and fourth column). Due to limited observations, our teeth do not receive vertex deformation. However, constraints on the teeth are considered during optimization to ensure compatibility with lip movements. This ensures that even when updating the expression basis for lip movements, there is no penetration with the teeth. In the supplementary video, we showcase the facial animations generated by the driven rig.

Novel-view synthesis. We demonstrate that our method can synthesize photo-realistic novel views, as shown in Fig. 8. Our method can accurately reconstruct the geometry and appearance of ears from sparse multi-view inputs, ensuring effective novel-view generalization for ear appearance and synthesizing high-quality ears (third column). Deferred rendering MLP is suitable for synthesizing photo-realistic facial appearance but cannot be directly imported into current animation software. Making deferred render-

ing MLP compatible with animation pipelines is a direction for future work. Recent efforts, such as those presented in [13, 44], are working towards achieving this goal. Our method relies on fast mesh-based rasterization and deferred neural rendering, enabling real-time animation and novel-view synthesis. In the supplementary video, we demonstrate real-time interactive control of the viewpoint.

5. Limitations

We aim to reconstruct personalized facial blendshapes from videos, enabling accurate surface geometry. However, surface geometry is suitable for modeling the skin but not ideal for modeling fine volumetric details like hair. In the animation pipeline, the focus is primarily on modeling the movement of facial muscles. Since hair is not in the region of muscle movement, its impact on animation is relatively small. However, future work could explore adopting a hybrid representation that uses different geometric forms to express facial skin and hair. This approach could lead to higher-quality rendering of face avatars. Our method optimizes per-frame head poses, while camera intrinsics and extrinsics are calibrated using a checkerboard pattern once before the capture. Recent works such as [41, 54] hold the potential to integrate with our method to achieve joint estimation of camera parameters. Our method can personalize template blendshapes. However, the ICT model [35] used in the experiment does not have a blendshape for the tongue, so the tongue modeling is not demonstrated. Future work could involve testing blendshapes for the tongue or designing a separate motion approach for the tongue.

6. Conclusion

We propose to reconstruct personalized blendshapes from RGB videos via neural inverse rendering, effectively addressing the gap between traditional animation pipelines and cutting-edge neural inverse rendering techniques. Leveraging a blendshape rig representation for dynamic facial modeling, we introduce a joint optimization process that refines the rig with per-vertex deformation schemes. This ensures seamless compatibility with animation pipelines and precise alignment with facial performances in RGB videos. Our contributions extend to an efficient inverse rendering framework that integrates neural shading with blendshapes, enabling the reconstruction of animation-ready facial rigs under diverse lighting and materials. A novel blendshape deformation technique, incorporating differential coordinates augmented with tetrahedral connections and semantic regularization, is introduced to enhance the expressiveness and adherence to volumetric Laplacian regularization. Experiments showcase the effectiveness of our approach in obtaining high-quality, animation-ready facial rigs from single or sparse multi-view videos, underscoring its accuracy and animation applicability.

References

- [1] Agisoft metashape professional (software). <http://www.agisoft.com/downloads/installer/>, 2023. Accessed: 2023-11-16. **5**
- [2] ShahRukh Athar, Zexiang Xu, Kalyan Sunkavalli, Eli Shechtman, and Zhixin Shu. Rignerf: Fully controllable neural 3d portraits. In *IEEE/CVF Conference on Computer Vision and Pattern Recognition, CVPR 2022, New Orleans, LA, USA, June 18-24, 2022*, pages 20332–20341. IEEE, 2022. **3, 6**
- [3] Thabo Beeler, Fabian Hahn, Derek Bradley, Bernd Bickel, Paul A Beardsley, Craig Gotsman, Robert W Sumner, and Markus H Gross. High-quality passive facial performance capture using anchor frames. *ACM Trans. Graph.*, 30(4):75, 2011. **1, 2**
- [4] Shrishya Bharadwaj, Yufeng Zheng, Otmar Hilliges, Michael J. Black, and Victoria Fernández Abrevaya. FLARE: fast learning of animatable and relightable mesh avatars. *CoRR*, abs/2310.17519, 2023. **3**
- [5] Volker Blanz and Thomas Vetter. A morphable model for the synthesis of 3d faces. In *Proceedings of the 26th Annual Conference on Computer Graphics and Interactive Techniques, SIGGRAPH 1999, Los Angeles, CA, USA, August 8-13, 1999*, pages 187–194. ACM, 1999. **2, 3**
- [6] Sofien Bouaziz, Yangang Wang, and Mark Pauly. Online modeling for realtime facial animation. *ACM Trans. Graph.*, 32(4):40:1–40:10, 2013. **2**
- [7] Derek Bradley, Wolfgang Heidrich, Tiberiu Popa, and Alla Sheffer. High resolution passive facial performance capture. *ACM Trans. Graph.*, 29(4):41:1–41:10, 2010. **2**
- [8] Hongrui Cai, Wanquan Feng, Xuetao Feng, Yan Wang, and Juyong Zhang. Neural surface reconstruction of dynamic scenes with monocular RGB-D camera. In *NeurIPS*, 2022. **3**
- [9] Chen Cao, Yanlin Weng, Stephen Lin, and Kun Zhou. 3d shape regression for real-time facial animation. *ACM Trans. Graph.*, 32(4):41:1–41:10, 2013. **1, 2**
- [10] Chen Cao, Qiming Hou, and Kun Zhou. Displaced dynamic expression regression for real-time facial tracking and animation. *ACM Trans. Graph.*, 33(4):43:1–43:10, 2014. **1, 2**
- [11] Chen Cao, Derek Bradley, Kun Zhou, and Thabo Beeler. Real-time high-fidelity facial performance capture. *ACM Trans. Graph.*, 34(4):46:1–46:9, 2015. **2**
- [12] Chen Cao, Vasu Agrawal, Fernando De la Torre, Lele Chen, Jason M. Saragih, Tomas Simon, and Yaser Sheikh. Real-time 3d neural facial animation from binocular video. *ACM Trans. Graph.*, 40(4):87:1–87:17, 2021. **2**
- [13] Zhiqin Chen, Thomas A. Funkhouser, Peter Hedman, and Andrea Tagliasacchi. Mobilenerf: Exploiting the polygon rasterization pipeline for efficient neural field rendering on mobile architectures. In *IEEE/CVF Conference on Computer Vision and Pattern Recognition, CVPR 2023, Vancouver, BC, Canada, June 17-24, 2023*, pages 16569–16578. IEEE, 2023. **8**
- [14] Blender Online Community. *Blender - a 3D modelling and rendering package*. Blender Foundation, Stichting Blender Foundation, Amsterdam, 2018. **2, 5, 8**
- [15] Artur Tavares de Carvalho Cruz and João Marcelo Xavier Natario Teixeira. A review regarding the 3d facial animation pipeline. In *SVR’21: 23rd Symposium on Virtual and Augmented Reality, Virtual Event, Brazil, October 18 - 21, 2021*, pages 192–196. ACM, 2021. **1**
- [16] Paul Debevec, Tim Hawkins, Chris Tchou, Haarm-Pieter Duiker, Westley Sarokin, and Mark Sagar. Acquiring the reflectance field of a human face. In *Proceedings of the 27th annual conference on Computer graphics and interactive techniques*, pages 145–156, 2000. **1**
- [17] Craig Donner and Henrik Wann Jensen. A spectral BSSRDF for shading human skin. In *Proceedings of the Eurographics Symposium on Rendering Techniques, Nicosia, Cyprus, 2006*, pages 409–417. Eurographics Association, 2006. **3**
- [18] Graham Fyffe, Koki Nagano, Loc Huynh, Shunsuke Saito, Jay Busch, Andrew Jones, Hao Li, and Paul E. Debevec. Multi-view stereo on consistent face topology. *Comput. Graph. Forum*, 36(2):295–309, 2017. **2**
- [19] Guy Gafni, Justus Thies, Michael Zollhöfer, and Matthias Nießner. Dynamic neural radiance fields for monocular 4d facial avatar reconstruction. In *Proceedings of the IEEE/CVF Conference on Computer Vision and Pattern Recognition (CVPR)*, pages 8649–8658, 2021. **1, 2, 3, 6**
- [20] Hang Gao, Ruilong Li, Shubham Tulsiani, Bryan Russell, and Angjoo Kanazawa. Monocular dynamic view synthesis: A reality check. In *NeurIPS*, 2022. **2, 4**
- [21] Xuan Gao, Chenglai Zhong, Jun Xiang, Yang Hong, Yudong Guo, and Juyong Zhang. Reconstructing personalized semantic facial nerf models from monocular video. *ACM Trans. Graph.*, 41(6):200:1–200:12, 2022. **3, 6**
- [22] Pablo Garrido, Levi Valgaerts, Chenglei Wu, and Christian Theobalt. Reconstructing detailed dynamic face geometry from monocular video. *ACM Trans. Graph.*, 32(6):158:1–158:10, 2013. **2**
- [23] Pablo Garrido, Michael Zollhöfer, Dan Casas, Levi Valgaerts, Kiran Varanasi, Patrick Pérez, and Christian Theobalt. Reconstruction of personalized 3d face rigs from monocular video. *ACM Transactions on Graphics (TOG)*, 35(3):1–15, 2016. **2**
- [24] Abhijeet Ghosh, Graham Fyffe, Borom Tunwattanapong, Jay Busch, Xueming Yu, and Paul Debevec. Multiview face capture using polarized spherical gradient illumination. *ACM Transactions on Graphics (TOG)*, 30(6):1–10, 2011. **1**
- [25] Philip-William Grassal, Malte Prinzler, Titus Leistner, Carsten Rother, Matthias Nießner, and Justus Thies. Neural head avatars from monocular RGB videos. In *IEEE/CVF Conference on Computer Vision and Pattern Recognition, CVPR 2022, New Orleans, LA, USA, June 18-24, 2022*, pages 18632–18643. IEEE, 2022. **1, 2, 3, 4, 6**
- [26] Alexandru Eugen Ichim, Sofien Bouaziz, and Mark Pauly. Dynamic 3d avatar creation from hand-held video input. *ACM Transactions on Graphics (ToG)*, 34(4):1–14, 2015. **2**
- [27] Hiroharu Kato, Deniz Beker, Mihai Morariu, Takahiro Ando, Toru Matsuoka, Wadim Kehl, and Adrien Gaidon. Differentiable rendering: A survey. *CoRR*, abs/2006.12057, 2020. **1**

- [28] Diederik P Kingma and Jimmy Ba. Adam: A method for stochastic optimization. *arXiv preprint arXiv:1412.6980*, 2014. 5
- [29] Tobias Kirschstein, Shenhan Qian, Simon Giebenhain, Tim Walter, and Matthias Nießner. Nersemble: Multi-view radiance field reconstruction of human heads. *ACM Trans. Graph.*, 42(4), 2023. 5, 6
- [30] Samuli Laine, Janne Hellsten, Tero Karras, Yeongho Seol, Jaakko Lehtinen, and Timo Aila. Modular primitives for high-performance differentiable rendering. *ACM Trans. Graph.*, 39(6):194:1–194:14, 2020. 2, 4, 5
- [31] John P. Lewis, Ken Anjyo, Taehyun Rhee, Mengjie Zhang, Frédéric H. Pighin, and Zhigang Deng. Practice and theory of blendshape facial models. In *35th Annual Conference of the European Association for Computer Graphics, Eurographics 2014 - State of the Art Reports, Strasbourg, France, April 7-11, 2014*, pages 199–218. Eurographics Association, 2014. 2, 3
- [32] Hao Li, Thibaut Weise, and Mark Pauly. Example-based facial rigging. *Acm transactions on graphics (tog)*, 29(4): 1–6, 2010. 2
- [33] Hao Li, Jihun Yu, Yuting Ye, and Chris Bregler. Realtime facial animation with on-the-fly correctives. *ACM Trans. Graph.*, 32(4):42:1–42:10, 2013. 2
- [34] Jiaman Li, Zhengfei Kuang, Yajie Zhao, Mingming He, Karl Bladin, and Hao Li. Dynamic facial asset and rig generation from a single scan. *ACM Trans. Graph.*, 39(6):215:1–215:18, 2020. 2
- [35] Ruilong Li, Karl Bladin, Yajie Zhao, Chinmay Chinara, Owen Ingraham, Pengda Xiang, Xinglei Ren, Pratusha Prasad, Bipin Kishore, Jun Xing, and Hao Li. Learning formation of physically-based face attributes. In *2020 IEEE/CVF Conference on Computer Vision and Pattern Recognition, CVPR 2020, Seattle, WA, USA, June 13-19, 2020*, pages 3407–3416. Computer Vision Foundation / IEEE, 2020. 5, 8
- [36] Shichen Liu, Weikai Chen, Tianye Li, and Hao Li. Soft rasterizer: A differentiable renderer for image-based 3d reasoning. In *2019 IEEE/CVF International Conference on Computer Vision, ICCV 2019, Seoul, Korea (South), October 27 - November 2, 2019*, pages 7707–7716. IEEE, 2019. 2
- [37] Luming Ma and Zhigang Deng. Real-time hierarchical facial performance capture. In *Proceedings of the ACM SIGGRAPH Symposium on Interactive 3D Graphics and Games, I3D 2019, Montreal, QC, Canada, May 21-23, 2019*, pages 11:1–11:10. ACM, 2019. 2
- [38] Ben Mildenhall, Pratul P. Srinivasan, Matthew Tancik, Jonathan T. Barron, Ravi Ramamoorthi, and Ren Ng. Nerf: Representing scenes as neural radiance fields for view synthesis. In *ECCV*, 2020. 1, 3
- [39] Thomas Müller, Alex Evans, Christoph Schied, and Alexander Keller. Instant neural graphics primitives with a multiresolution hash encoding. *ACM Trans. Graph.*, 41(4):102:1–102:15, 2022. 4
- [40] Baptiste Nicolet, Alec Jacobson, and Wenzel Jakob. Large steps in inverse rendering of geometry. *ACM Transactions on Graphics (Proceedings of SIGGRAPH Asia)*, 40(6), 2021. 4, 5
- [41] Keunhong Park, Philipp Henzler, Ben Mildenhall, Jonathan T. Barron, and Ricardo Martin-Brualla. Camp: Camera preconditioning for neural radiance fields. *CoRR*, abs/2308.10902, 2023. 8
- [42] Ekman Paul and Wallace V Friesen. Facial action coding system: a technique for the measurement of facial movement. *Consulting Psychologists*, 1978. 4
- [43] Nikhila Ravi, Jeremy Reizenstein, David Novotný, Taylor Gordon, Wan-Yen Lo, Justin Johnson, and Georgia Gkioxari. Accelerating 3d deep learning with pytorch3d. *CoRR*, abs/2007.08501, 2020. 2
- [44] Christian Reiser, Richard Szeliski, Dor Verbin, Pratul P. Srinivasan, Ben Mildenhall, Andreas Geiger, Jonathan T. Barron, and Peter Hedman. MERF: memory-efficient radiance fields for real-time view synthesis in unbounded scenes. *ACM Trans. Graph.*, 42(4):89:1–89:12, 2023. 8
- [45] Ruizhi Shao, Zerong Zheng, Hanzhang Tu, Boning Liu, Hongwen Zhang, and Yebin Liu. Tensor4d: Efficient neural 4d decomposition for high-fidelity dynamic reconstruction and rendering. In *IEEE/CVF Conference on Computer Vision and Pattern Recognition, CVPR 2023, Vancouver, BC, Canada, June 17-24, 2023*, pages 16632–16642. IEEE, 2023. 3
- [46] Hang Si. Tetgen, a delaunay-based quality tetrahedral mesh generator. *ACM Trans. Math. Softw.*, 41(2), 2015. 4, 5
- [47] Olga Sorkine and Marc Alexa. As-rigid-as-possible surface modeling. In *Proceedings of the Fifth Eurographics Symposium on Geometry Processing*, page 109–116, Goslar, DEU, 2007. Eurographics Association. 5
- [48] Olga Sorkine, Daniel Cohen-Or, Yaron Lipman, Marc Alexa, Christian Rössl, and Hans-Peter Seidel. Laplacian surface editing. In *Second Eurographics Symposium on Geometry Processing, Nice, France, July 8-10, 2004*, pages 175–184. Eurographics Association, 2004. 4
- [49] Robert W Sumner and Jovan Popović. Deformation transfer for triangle meshes. *ACM Transactions on graphics (TOG)*, 23(3):399–405, 2004. 2
- [50] Matthew Tancik, Pratul P. Srinivasan, Ben Mildenhall, Sara Fridovich-Keil, Nithin Raghavan, Utkarsh Singhal, Ravi Ramamoorthi, Jonathan T. Barron, and Ren Ng. Fourier features let networks learn high frequency functions in low dimensional domains. In *Advances in Neural Information Processing Systems 33: Annual Conference on Neural Information Processing Systems 2020, NeurIPS 2020, December 6-12, 2020, virtual*, 2020. 4
- [51] Ayush Tewari, Justus Thies, Ben Mildenhall, Pratul P. Srinivasan, Edgar Tretschk, Yifan Wang, Christoph Lassner, Vincent Sitzmann, Ricardo Martin-Brualla, Stephen Lombardi, Tomas Simon, Christian Theobalt, Matthias Nießner, Jonathan T. Barron, Gordon Wetzstein, Michael Zollhöfer, and Vladislav Golyanik. Advances in neural rendering. *Comput. Graph. Forum*, 41(2):703–735, 2022. 1
- [52] Justus Thies, Michael Zollhöfer, Marc Stamminger, Christian Theobalt, and Matthias Nießner. Face2face: Real-time face capture and reenactment of RGB videos. In *2016 IEEE Conference on Computer Vision and Pattern Recognition, CVPR 2016, Las Vegas, NV, USA, June 27-30, 2016*, pages 2387–2395. IEEE Computer Society, 2016. 1, 2

- [53] Justus Thies, Michael Zollhöfer, and Matthias Nießner. Deferred neural rendering: image synthesis using neural textures. *ACM Trans. Graph.*, 38(4):66:1–66:12, 2019. 3
- [54] Prune Truong, Marie-Julie Rakotosaona, Fabian Manhardt, and Federico Tombari. SPARF: neural radiance fields from sparse and noisy poses. In *IEEE/CVF Conference on Computer Vision and Pattern Recognition, CVPR 2023, Vancouver, BC, Canada, June 17-24, 2023*, pages 4190–4200. IEEE, 2023. 8
- [55] Levi Valgaerts, Chenglei Wu, Andrés Bruhn, Hans-Peter Seidel, and Christian Theobalt. Lightweight binocular facial performance capture under uncontrolled lighting. *ACM Trans. Graph.*, 31(6):187:1–187:11, 2012. 2
- [56] Carlos Vilchis, Carmina Pérez-Guerrero, Mauricio Mendez-Ruiz, and Miguel González-Mendoza. A survey on the pipeline evolution of facial capture and tracking for digital humans. *Multim. Syst.*, 29(4):1917–1940, 2023. 1
- [57] Daniel Vlasic, Matthew Brand, Hanspeter Pfister, and Jovan Popovic. Face transfer with multilinear models. *ACM Trans. Graph.*, 24(3):426–433, 2005. 2
- [58] Zhibo Wang, Jingwang Ling, Chengzeng Feng, Ming Lu, and Feng Xu. Emotion-preserving blendshape update with real-time face tracking. *IEEE Transactions on Visualization and Computer Graphics*, 28(6):2364–2375, 2020. 2
- [59] Thibaut Weise, Sofien Bouaziz, Hao Li, and Mark Pauly. Realtime performance-based facial animation. *ACM Trans. Graph.*, 30(4):77, 2011. 2
- [60] Markus Worchel, Rodrigo Diaz, Weiwen Hu, Oliver Schreer, Ingo Feldmann, and Peter Eisert. Multi-view mesh reconstruction with neural deferred shading. In *IEEE/CVF Conference on Computer Vision and Pattern Recognition, CVPR 2022, New Orleans, LA, USA, June 18-24, 2022*, pages 6177–6187. IEEE, 2022. 3
- [61] Markus Worchel, Rodrigo Diaz, Weiwen Hu, Oliver Schreer, Ingo Feldmann, and Peter Eisert. Multi-view mesh reconstruction with neural deferred shading. In *Proceedings of the IEEE/CVF Conference on Computer Vision and Pattern Recognition (CVPR)*, pages 6187–6197, 2022. 4
- [62] Fanzi Wu, Linchao Bao, Yajing Chen, Yonggen Ling, Yibing Song, Songnan Li, King Ngi Ngan, and Wei Liu. Mvf-net: Multi-view 3d face morphable model regression. In *CVPR*, 2019. 6
- [63] Cheng-hsin Wu, Ningyuan Zheng, Scott Ardisson, Rohan Bali, Danielle Belko, Eric Brockmeyer, Lucas Evans, Timothy Godisart, Hyowon Ha, Xuhua Huang, Alexander Hypes, Taylor Koska, Steven Krenn, Stephen Lombardi, Xiaomin Luo, Kevyn McPhail, Laura Millerschoen, Michal Perdoch, Mark Pitts, Alexander Richard, Jason Saragih, Junko Saragih, Takaaki Shiratori, Tomas Simon, Matt Stewart, Autumn Trimble, Xinshuo Weng, David Whitewolf, Chenglei Wu, Shou-I Yu, and Yaser Sheikh. Multiface: A dataset for neural face rendering. In *arXiv*, 2022. 5, 6
- [64] Yuelang Xu, Lizhen Wang, Xiaochen Zhao, Hongwen Zhang, and Yebin Liu. Avatarmav: Fast 3d head avatar reconstruction using motion-aware neural voxels. In *ACM SIGGRAPH 2023 Conference Proceedings, SIGGRAPH 2023, Los Angeles, CA, USA, August 6-10, 2023*, pages 47:1–47:10. ACM, 2023. 3, 6
- [65] Haotian Yang, Hao Zhu, Yanru Wang, Mingkai Huang, Qiu Shen, Ruigang Yang, and Xun Cao. Facescape: A large-scale high quality 3d face dataset and detailed riggable 3d face prediction. In *2020 IEEE/CVF Conference on Computer Vision and Pattern Recognition, CVPR 2020, Seattle, WA, USA, June 13-19, 2020*, pages 598–607. Computer Vision Foundation / IEEE, 2020. 2
- [66] Yufeng Zheng, Victoria Fernández Abrevaya, Marcel C. Bühler, Xu Chen, Michael J. Black, and Otmar Hilliges. I M Avatar: Implicit morphable head avatars from videos. In *Computer Vision and Pattern Recognition (CVPR)*, 2022. 1, 3, 6
- [67] Yinglin Zheng, Hao Yang, Ting Zhang, Jianmin Bao, Dongdong Chen, Yangyu Huang, Lu Yuan, Dong Chen, Ming Zeng, and Fang Wen. General facial representation learning in a visual-linguistic manner. In *Proceedings of the IEEE/CVF Conference on Computer Vision and Pattern Recognition*, pages 18697–18709, 2022. 5
- [68] Yufeng Zheng, Wang Yifan, Gordon Wetzstein, Michael J. Black, and Otmar Hilliges. Pointavatar: Deformable point-based head avatars from videos. In *Proceedings of the IEEE/CVF Conference on Computer Vision and Pattern Recognition (CVPR)*, 2023. 1, 3, 4, 6
- [69] Wojciech Zielonka, Timo Bolkart, and Justus Thies. Instant volumetric head avatars. In *IEEE/CVF Conference on Computer Vision and Pattern Recognition, CVPR 2023, Vancouver, BC, Canada, June 17-24, 2023*, pages 4574–4584. IEEE, 2023. 1, 2, 3, 6